Small Structures

small structures

www.small-structures.com

RESEARCH ARTICLE OPEN ACCESS

Preferential Alkali-Ion Occupation in NASICON Cathodes Enables High-Power Sodium-Ion Batteries

Hongsheng Han[1] | Ruifu Li[1] | Kaidi Wang[2] | Hongxu Qu[1] | Huihua Li[1] | Minghua Chen[1] | Huang Zhang[1] | Stefano Passerini[2,3]

[1]School of Electrical and Electronic Engineering, Key Laboratory of Engineering Dielectric and Applications (Ministry of Education), Harbin University of Science and Technology, Harbin, P. R. China | [2]Karlsruhe Institute of Technology, Helmholtz Institute Ulm (HIU), Ulm, Germany | [3]Center for Transport Technologies, Austrian Institute of Technology (AIT), Wien, Austria

Correspondence: Huang Zhang (zhang.huang@hrbust.edu.cn) | Stefano Passerini (stefano.passerini@kit.edu)

Received: 31 October 2025 | **Revised:** 6 January 2026 | **Accepted:** 7 January 2026

Keywords: high power density | $Na_3V_2(PO_4)_3$ | polyanionic cathodes | preferential alkali-ion occupation | sodium-ion batteries

ABSTRACT

Sodium-ion batteries (SIBs) are gaining attention as promising large-scale energy storage systems due to their cost-effectiveness and resource abundance. As a cathode material, NASICON-type $Na_3V_2(PO_4)_3$ (NVP) stands out for its high structural stability and energy density. However, its practical application is hindered by poor electronic conductivity and sluggish Na^+ diffusion kinetics. In this study, we systematically investigated the structural evolution and Na^+ storage behavior of NVP materials, particularly focusing on enhancing power capability through preferential substitution of Na^+ with other alkali metal ions (K^+ and Li^+). Results show that preferential K^+ occupation at (6b) Na1 sites can manipulate the crystal structure and regulate Na^+ migration behaviors, significantly influencing the energy efficiency, rate performance, and cycling stability. Consequently, the K^+-substituted material (NKVP) delivers, at room temperature, a discharge capacity of 80.6 mAh g^{-1} at the ultrahigh rate of 100C but also retains 80.8% of its capacity over 10,000 cycles at 50C, along with superior high-temperature cycling stability over 3000 cycles at 10C and 60°C. Practically, the NKVP//HC full cell exhibits superior power performance. This work provides critical insights into the rational design of high-performance NASICON materials, offering new pathways for the development of high-power SIBs.

1 | Introduction

Renewable energy sources such as solar and wind power are key drivers of green and sustainable development, while these energy sources are highly dependent on natural conditions [1–3]. In this context, developing efficient, low-cost, and eco-friendly energy storage technologies is crucial for effectively storing and utilizing renewable energy [3]. Among various energy storage technologies, lithium-ion battery (LIB) stands out in large-scale energy storage systems due to its high energy density and efficiency [4]. Yet, the scarcity of lithium resources has significantly constrained the development of LIBs. In contrast, sodium-ion batteries (SIBs) present a new opportunity for large-scale energy storage systems, which has abundant resources and shares chemical similarities with lithium [5–10].

Polyanionic compounds, as cathode materials, have recently garnered significant attention for sodium ion batteries, due to their stable cycling performance, excellent rate capability, high theoretical capacity, high operating voltage plateau, and good thermal stability [11–14]. $Na_3V_2(PO_4)_3$ (NVP), with its 3D open structure enabling rapid Na ion migration, belonging to the R-3c space group with a 3D framework interlinked by VO_6 octahedra and PO_4 tetrahedra sharing corners, is a very promising candidate [15–17]. In this material, Na^+ ions occupy two distinct sites, i.e., six-coordinated Na(1) site at the intersection of the 3D channel

and eight-coordinated Na(2) site inside the channel [18–20]. During the de-sodiation process, all outer sodium ions originate from the Na(2) site, while the Na(1) site remains unchanged. Even after losing two sodium ions, the NVP framework remains stable due to the strong covalent effect of $(PO_4)^{3-}$, delivering a high capacity of 117.6 mAh g^{-1}. The Na(1) site is located at a longer distance from the V-O layer and is less affected by the redox activity of V, whereas the Na(2) site is closer to the V-O layer and exhibits stronger redox activity. However, the framework structure composed of PO_4 and VO_6 groups severely restricts the electronic conductivity, resulting in poor rate performance and low cycling stability.

Recently, ion substitution within the crystal structure has proven to be an efficient strategy, attributed to the diverse sites available for ion occupation [21, 22]. For example, substitution with Al at the V site can enhance the electronic conductivity and structural stability of the cathode material [20, 23]. In Al-doped NVP/C cathodes, the Al^{3+} ions occupying the V sites improve the electronic conductivity of the material and suppress the dissolution of V ions during charge–discharge, enabling excellent cycling stability and rate performance. Indeed, various transition metals have been adopted to partially substitute V in the NVP crystal structure to improve its long-term cycling stability [24–28]. Meanwhile, the ion substitution can also take place at the anion sites. It has been reported that the F^- substitution at PO_4-site can increase the working potential of NVP materials, due to the high electronegativity of F^- causing a strong inductive effect [29]. Mai et al. also adopted the co-substitution structure at both V-site and PO_4-site to enhance the cycling stability and multiplicity performance of the NVP materials by simultaneously substituting Al and F [27]. The cation (Fe^{3+}) and multivalent anion group (MoO_4^{2-}) are also co-doped into NVP by replacing V^{3+} and PO_4^{3-}, remarkably promote the sodium-ion de/intercalation potential and specific capacity compared to pristine NVP [30]. The two Na^+ sites in NVP serve distinct functions in ion transport and structural maintenance. Selective ion substitution at these sites with suitable alkali metals effectively expands the diffusion pathways and stabilizes the host lattice, thereby reducing the overall migration energy barrier for Na^+. Indeed, the trace amount of K^+ substitution, i.e., $Na_{2.95}K_{0.05}V_2(PO_4)_3$, has been reported to improve the Na (de)intercalation kinetics and structural stability, thus contributing to high rate performance [31]. However, while such enhancements are documented, the precise structure-property relationship governed by site-selective alkali-ion occupation remains elusive.

In this work, we conducted a systematic investigation into the structural evolution and Na^+ storage behavior of NVP materials, with a particular emphasis on enhancing their power capability through preferential substitution of Na with alkali metal ions (K^+ and Li^+). The typical NASICON-type $Na_{3-x}M_xV_2(PO_4)_3$ ($x = 0$, 0.5; M = K, Li) cathode materials were synthesized via conventional sol–gel method. Electrochemical tests showed that both K^+ and Li^+ substitutions can boost the power capability and cycling stability of NVP cathodes. Notably, the K^+-substituted NKVP material delivered exceptional power performance with superior energy efficiency and long lifespan in both half- and full-cells. In-depth theoretical and structural analyses verified that K^+ ions preferentially occupy the Na1(6b) site in NVP structure, which significantly facilitates the intrinsic ion diffusion capability in the materials, thereby enhancing high-power sodium storage capability.

2 | Results and Discussion

The $Na_{3-x}M_xV_2(PO_4)_3$ ($x = 0$, 0.5; M = K, Li) materials were synthesized via sol–gel method (experimental details in Supporting Information) and named as NVP, NKVP, and NLVP, respectively. The X-ray diffraction (XRD) patterns of NVP, NLVP, and NKVP powders are illustrated in Figure 1a. All samples showed distinct diffraction peaks related to the NASICON structure with the space group R3-c [32]. The magnified XRD patterns (Figure 1b) show that the K^+ substitution at Na sites induces the shift of the (104) peak at 20.1° and (113) peak at 23.7° to lower 2θ values, indicating the lattice expansion due to the large radius of K^+ (133 pm) than Na^+ (102 pm) [33–36]. Notably, it can be seen that NKVP showed relatively small diffraction peaks at 2θ 15°, 30.8°, and 33.4°, which can be indexed to the K-based pyrophosphates due to the excessive substitution and sintering temperature [37].

To further investigate the preferential occupation of the alkali cations and their induced lattice parameter changes, Rietveld refinement was performed on the XRD patterns of NVP, NLVP, and NKVP, as displayed in Figures S1 and S2 and 1c, respectively. The detailed lattice parameters are listed in Table S1. Compared to NVP, NKVP showed a slight contraction in the *a*- and *b*-axis (with the *a*-axis equal to the *b*-axis), whereas the *c*-axis undergoes a significant expansion. Consequently, the lattice volume increases to 1444.2 $Å^3$. This enlargement of the lattice affords large channels for Na^+ diffusion in the bulk, which is beneficial to reduce the migration energy barrier of Na^+ during (de-)sodiation [33]. Furthermore, atomic occupancy information for NVP, NLVP and NKVP was obtained from Rietveld refinement, as listed in Tables S2–S4. It can be observed that K^+ substitution exhibits a preference for occupying the Na1 site in the NVP, while the Li^+ substitution takes place at both Na1 and Na2 sites. Figure 1d illustrates the schematic crystal structure of NKVP, in which the green octahedra represent the $[VO_6]$ units, the lavender tetrahedra represent the $[PO_4]$ groups. Na^+ ions occupy the six-coordinated (6b) Na1 sites and eight-coordinated (18e) Na2 sites, depicted in orange and yellow, respectively. The K^+ ions in deep purple are positioned at the six-coordinated (6b) Na1 sites.

Thermogravimetric (TG) analysis in Figure 1e shows the carbon contents in NVP, NLVP, and NKVP composites to be approximately 5.1%, 5.3%, and 4.2%, respectively, stemming from organic acids and salts decomposition [38]. Raman spectroscopy results of NVP, NLVP, and NKVP are shown in Figure 1f. The I_D/I_G ratios of NVP, NLVP and NKVP are calculated to be 1.03, 1.03, and 1.02, respectively, indicating that the alkali-ions substitution did not significantly affect the nature of pyrolytic carbon in the NVP composites [39]. Scanning electron microscopy (SEM) and high-resolution transmission electron microscopy (HR-TEM) were used to examine the morphology and crystallography of NKVP. As shown in Figure 1g and Figure S3, both NKVP and NVP exhibit a uniform porous structure. This microstructure enhances the electrode–electrolyte contact area, thereby contributing to the improved rate performance [16]. Figure 1h presents the TEM image of NKVP, confirming the porous structure with NVP particles embedded in the carbon matrix. HR-TEM images (Figure 1i) reveal an amorphous carbon layer uniformly coating the surface of NVKP particles, which is beneficially enhancing the electrical conductivity of the material (Figure 1i) [26]. The lattice fringes with spacings of 0.46 nm and 0.252 nm correspond

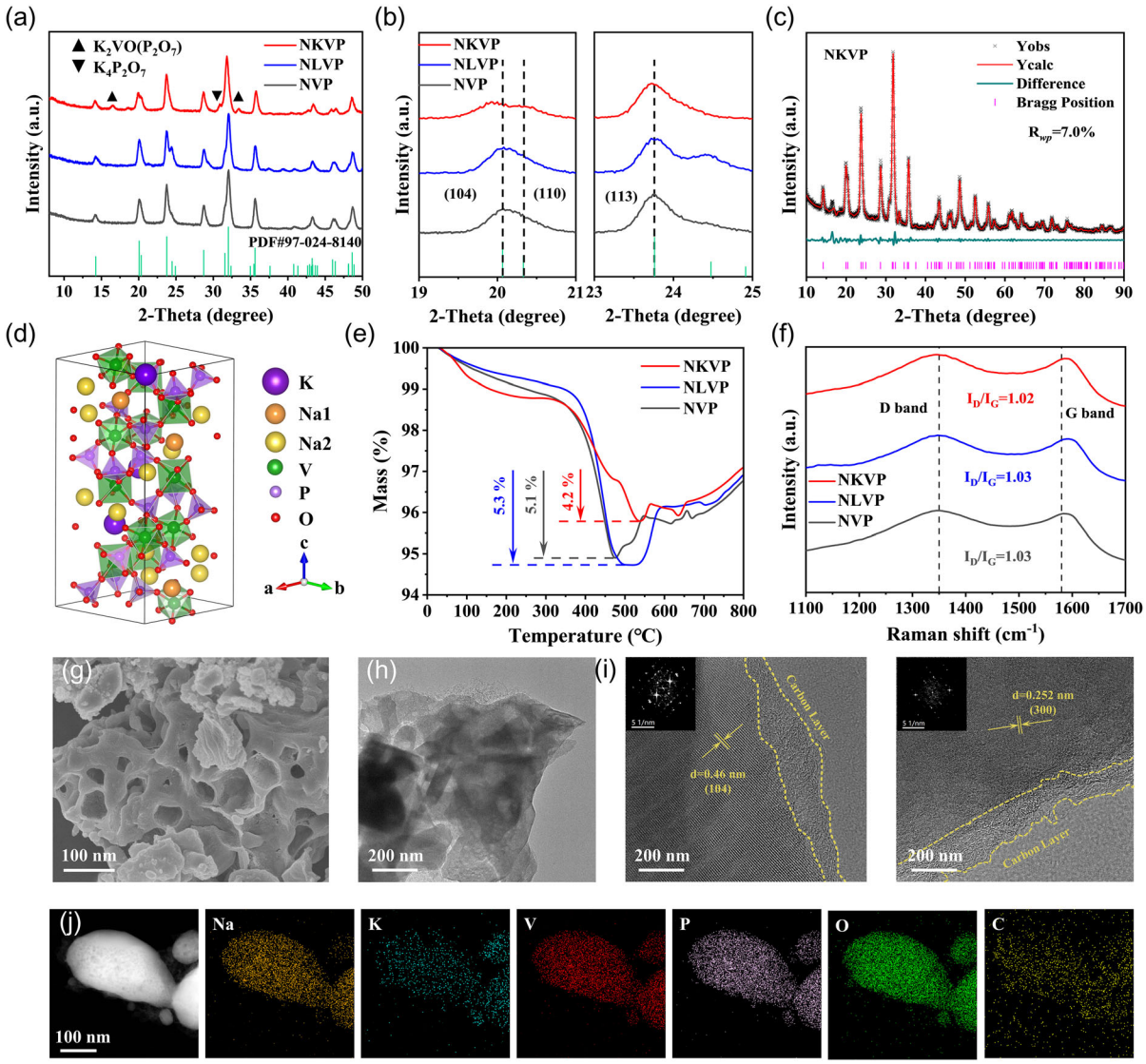

FIGURE 1 | (a,b) X-ray diffraction patterns and selected magnified areas. (c) Rietveld refinement of NKVP. (d) Theoretical crystal structure of NKVP. (e) TGA curves. (f) Raman spectra. (g–i) SEM, TEM, and HRTEM and FFT images of NKVP. (j) TEM elemental mapping results of NKVP.

well to the (104) and (300) crystal planes of NKVP, respectively. Compared to the XRD standard card of NVP (PDF#97-024-8140), the lattice spacing of NKVP in the (104) crystal plane is widened by approximately 0.18 Å due to K^+ substitution, thus enlarging the ion diffusion channels [28]. This aligns with the XRD and fast Fourier transform (FFT) patterns results, confirming the successful incorporation of K^+ into the lattice. The energy dispersive spectroscopy (EDS) mapping results show the uniform distribution of Na, K, V, P, O, and C elements in NKVP (Figure 1j). These results clearly demonstrate the successful synthesis of NVP materials with preferential occupancy and uniform substitution of alkali ions.

To investigate the effects of different alkali ion substitutions on the Na^+ storage performance, half-cell tests were performed on the NVP, NLVP, and NKVP cathode materials using Na metal as the counter electrode. Figure 2a demonstrates the typical galvanostatic charge/discharge (GCD) curves of NVP, NLVP, and NKVP materials at 0.5C (1C = 100 mA g^{-1}), showing the distinct voltage plateau based on V^{3+}/V^{4+} redox reaction at around 3.4 V. The specific discharge capacities are 107.4 mAh g^{-1} for NVP, 117.6 mAh g^{-1} for NLVP, and 103.6 mAh g^{-1} for NKVP. Notably, all three materials exhibit a second plateau, with NLVP exhibiting the longest. This second plateau at ~3.1 V can be attributed to the coexistence of two phases with the ordering of vacancy arrangements at the end of discharge generating structural mismatch and significant kinetic limitations. This increases the migration energy barriers of sodium ions during the two-phase reaction, thereby leading to polarization, i.e., voltage drop [38, 40–43]. Therefore, the second plateau in the discharge curve directly reflects the Na^+ ion diffusion behavior related to the energy barriers. Comparing the three materials, NKVP demonstrates the shortest plateau, suggesting that K^+ substitution can optimize the Na^+ diffusion pathways and reduce the migration energy barriers more effectively than Li^+ substitution. This finding underscores the significant impact of alkali metal substitution on Na^+ diffusion kinetics in NVP-based cathode materials. In this context, the rate capability tests of NVP, NLVP, and NKVP were conducted from 0.5C to 100C (Figure S4). The specific discharge capacities at 0.5C were used as the benchmark for data normalization, yielding the capacity retention plots under various

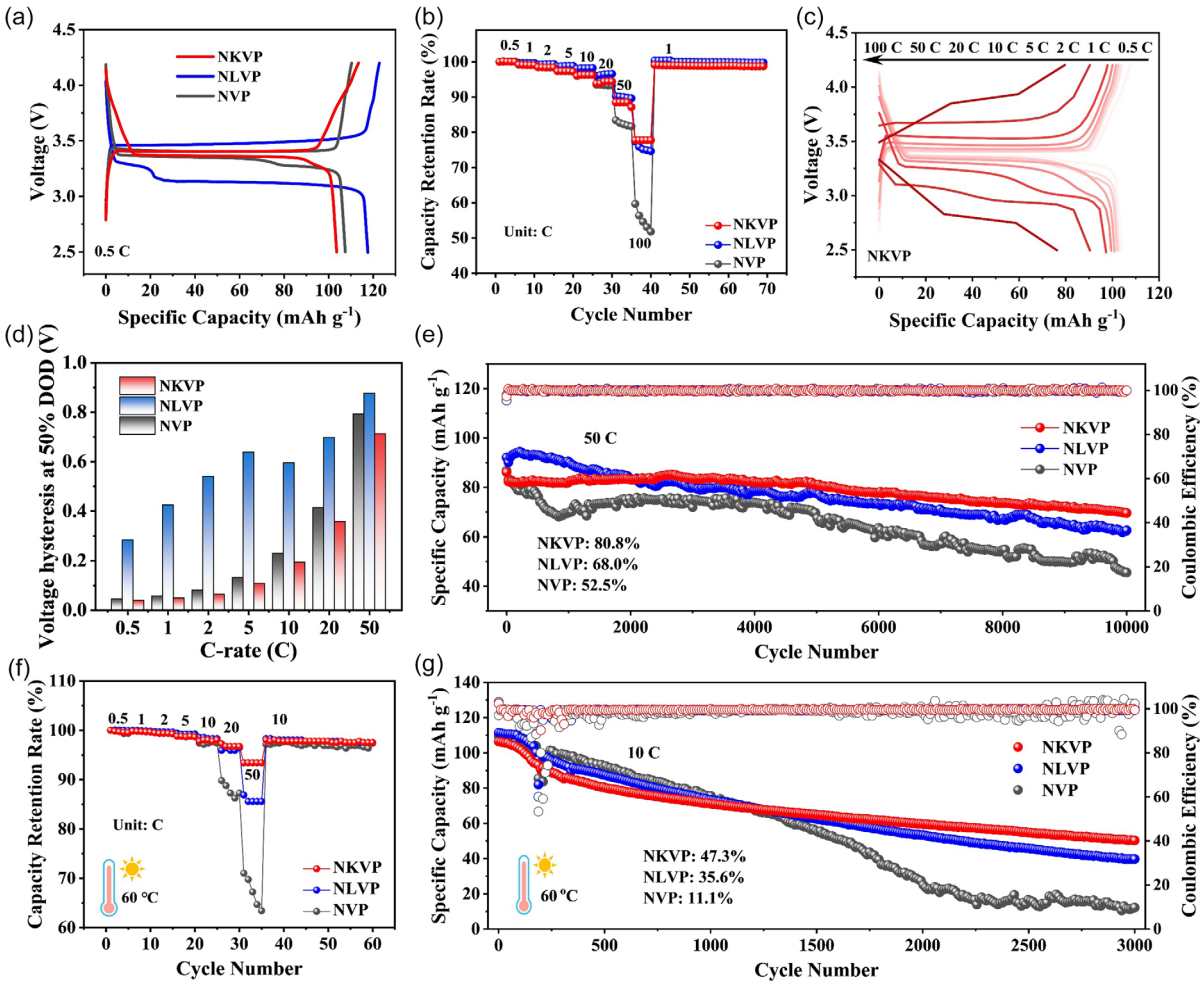

FIGURE 2 | Electrochemical performance of NVP, NLVP, and NKVP. (a) First cycle GCD curves between 2.5–4.2 V at 0.5C and . (b) Capacity retention at various current rates from 0.5C to 100C. (c) GCD curves of NKVP at various C-rates. (d) Voltage hysteresis at 50% depth-of-discharge (DOD) from the charge–discharge profiles of NVP, NLVP, and NKVP at various C-rates. (e) The cycling performances at 50C. (f,g) Rate performance and cycling performance at 10C and high-temperature (60°C).

C-rates (Figure 2b). NLVP and NKVP exhibited superior rate performance compared to the pristine NVP, and the capacity retentions at 50C were 90.0% for NLVP, and 88.5% for NKVP, respectively, higher than that of NVP (82.3%). Remarkably, at an ultrahigh rate of 100C, NKVP retained 77.8% of its 0.5C capacity, which translates to a practical charging time of approximately 0.47 min, whereas NVP and NLVP suffered severe decay. To verify the robustness of this exceptional rate performance, two independent replicate tests were conducted on NKVP, confirming the high reproducibility of the results (Figure S5). Figure 2c and S6–7 display the selected GCD curves of NKVP, NVP, and NLVP from 0.5C to 50C. It is seen that NKVP exhibits lower polarization and a shorter second plateau compared to the NVP and NLVP at high rates. These results clearly demonstrate the exceptional high-rate performance of NKVP due to facilitated Na^+ diffusion kinetics. To evaluate practical applicability, the rate performance of NVP and NKVP was assessed under high-mass-loading conditions (~5 mg cm^{-2}). The data (Figure S8) confirm the sustained kinetic superiority of NKVP over NVP.

The voltage hysteresis was calculated based on the voltage profiles at various C-rates (Figure 2d), defined as the voltage difference between the charge and discharge curves at 50% state-of-charge (SOC) and 50% DOD. This difference reflects the degree of polarization relative to the equilibrium potential, where a larger hysteresis indicates greater polarization and higher energy loss [38, 44]. NLVP shows the highest voltage hysteresis across various C-rates, which can be ascribed to the prolonged second voltage plateau below 3.4 V. For pristine NVP, the voltage hysteresis gradually increases as the C-rate rises. Notably, NKVP has the smallest voltage hysteresis at all C-rates, indicating the least polarization and energy loss during Na^+ insertion/extraction resulting from the K^+ substitution which enlarges ion transport channels and lowers Na^+ migration energy barriers [33]. To specifically exhibit the energy losses caused by polarization, Figure S9 presents the energy efficiencies of NVP, NLVP, and NKVP at different C-rates. It is noteworthy that NKVP exhibits the highest energy efficiency across various charge/discharge rates, further confirming its superior rate performance with the highest reversible capacity among all materials. The long-term cycling tests at 50C were conducted, as shown in Figure 2e. Notably, NKVP electrode demonstrates remarkable stability, delivering a reversible capacity of 86.12 mAh g^{-1} at 50C with 80.8% capacity retention after 10,000 cycles at room temperature. This corresponds to a minimal decay rate of 0.0019% per cycle.

In contrast, NVP electrode had an initial capacity of 86.81 mAh g^{-1} but exhibited rapid capacity fading after 360 cycles, resulting in a capacity retention of only 52.5% after 10,000 cycles. NLVP electrode, while outperforming NKVP with an initial capacity of 92.09 mAh g^{-1}, only delivered a capacity retention of 68.0%, i.e., much lower than that of NKVP. It is seen that the K^+ substitution can efficiently improve the cycling stability of NASICON materials at high rate, showing its potential for high power applications.

At high temperature, the compatibility between NASICON-type cathodes and electrolytes becomes a critical issue, further destabilizing the structure and degrading electrochemical performance [45, 46]. To evaluate the high-temperature performance of NVP, NLVP, and NKVP, the cells were tested at 60°C, and the capacity retentions at various C-rates are shown in Figure 2f. At 50C rate test, NKVP delivered a capacity retention of 93.4% with respect to the initial capacity delivered at 0.5C. In contrast, NVP rapidly degraded at high rate (i.e., above 20C), which can be attributed to the accelerated decomposition and side effects at high temperature [47–49]. The capacity retention of NLVP at 50C is 85.5%, outperforming NVP but lower than NKVP. Figure 2g further illustrated the long-term cycling tests of NVP, NLVP, and NKVP electrodes at 60°C and 10C, with capacity retention after 3000 cycles of 11.1%, 35.6%, and 47.3%, respectively. These results confirm that K^+ substitution enables the NKVP electrode to maintain outstanding high-power and long-term cycling performance even at elevated temperatures.

In situ XRD measurements were used to probe the structural evolution of NKVP during electrochemical cycling. Figure 3a presents the in situ XRD patterns alongside the corresponding charge–discharge profiles for the first and second cycles. During the initial charging phase (Na^+ deintercalation), all the distinct diffraction peaks correspond exclusively to the $Na_{2.5}K_{0.5}V_2(PO_4)_3$ phase (NASICON structure, space group R$\bar{3}$c). Upon further charging, the diffraction peaks shift abruptly to higher angles, concomitant with the emergence of a new phase, identified as $NaV_2(PO_4)_3$ phase [17, 32, 40]. Critically, the subsequent discharge process (Na^+ intercalation) reveals a fully reversible phase transformation, with the $Na_{0.5}K_{0.5}V_2(PO_4)_3$ phase reversibly converting back to the initial $Na_{2.5}K_{0.5}V_2(PO_4)_3$ phase. The diffraction peak evolution in the second cycle closely replicates that of the first cycle, unequivocally demonstrating the exceptional structural reversibility of NKVP. Significantly, NKVP achieves highly efficient Na^+

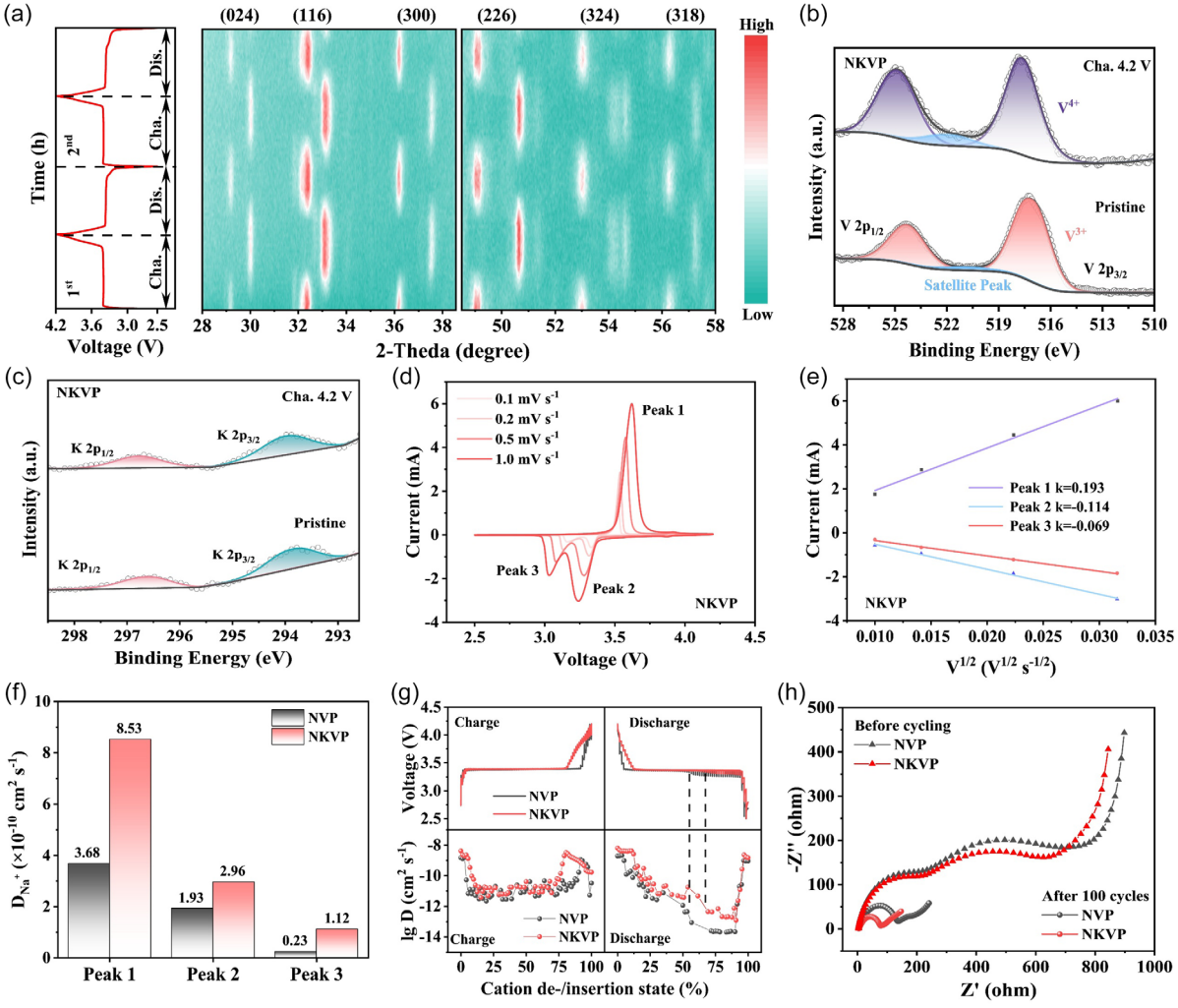

FIGURE 3 | Structural evolution and electrochemical dynamics. (a) In situ XRD contour pattern. (b,c) Ex situ XPS spectra of V 2p and K 2p of NKVP recorded on the electrodes at pristine (OCV) electrode and electrode at charged state (4.2 V). (d) CV curves at different scan rates of NKVP. (e) The linear relationship between i_p and $v^{1/2}$ from CV profiles of NKVP. (f) D_{Na+} values obtained from CV curves. (g) GITT curves and the corresponding ions diffusion coefficients. (h) EIS spectra of NVP and NKVP before cycling (at OCV after 12 h rest) and after 100 cycles (discharged state at 2.5 V).

deintercalation/intercalation reactions via this robust and highly reversible two-phase transformation, showing an excellent correlation with the observed electrochemical performance [32, 38, 40].

To further elucidate the role of K substitution in redox reaction mechanism during Na^+ de-/intercalation, X-ray photoelectron spectroscopy (XPS) was used to analyze the chemical valence changes of V and K in pristine and charged NKVP cathodes (Figures S10–S12 and 3b,c). For pristine NKVP, the V $2p_{3/2}$ and V $2p_{1/2}$ peaks are observed at binding energies of 517.06 eV and 524.27 eV, respectively, confirming the vanadium oxidation state as V^{3+} [50]. Upon charging to 4.2 V (Figure 3b), these peaks shift to higher binding energies of 517.63 eV and 524.87 eV, testifying the complete oxidation of V^{3+} to V^{4+} [26]. Critically, the K $2p_{3/2}$ and K $2p_{1/2}$ binding energies (Figure 3c) remain spectroscopically inert throughout the charging process, suggesting that K^+ remains electrochemically inactive during the V^{3+}/V^{4+} redox. These findings confirm that K^+ occupying the Na(1) sites, serves as a structural stabilizing agent ('pillar'), facilitating the highly reversible Na^+ transport via the intrinsic V^{3+}/V^{4+} redox mechanism without participating electrochemically [21, 35].

Building upon the established enhancements in electrochemical performance and structural stability imparted by K^+ substitution, a comprehensive kinetic analysis using cyclic voltammetry (CV), galvanostatic intermittent titration technique (GITT), and electrochemical impedance spectroscopy (EIS) was undertaken to probe Na^+ diffusion kinetics. Figures S13, S14 and 3d present the CV profiles of NVP, NLVP, and NKVP at scan rates from 0.1 to 1 mV s^{-1}. It is evident that NLVP demonstrates the largest voltage gap between the oxidation peak and the reduction peak, confirming its highest voltage hysteresis consistently with the GCD profiles. While the voltage gap slightly increases with scan rate for both NVP and NKVP, this latter exhibits a markedly smaller increase compared to the former, indicating that the electrochemical activity and the reversibility of the redox reaction are enhanced by K^+ substitution [16]. Notably, the CV curves clearly exhibit one oxidation peak and two reduction peaks, among which the second reduction peak at low voltage (peak 3) contributes to the energy loss due to the voltage polarization [38, 40–43]. Crucially, the peak is significantly less prominent in NKVP than NVP, which directly reflects the lower migration energy barrier encountered by Na^+ within the K^+-stabilized NKVP framework during the latter stages of discharge (Na1 to Na2). In contrast, the more pronounced voltage hysteresis in NLVP, stemming from a higher energy barrier within its constrained migration pathways, manifests as a distinct broadening of the redox features [16, 17, 40–43].

The linear relationship between the square root of the scan rate ($v^{1/2}$) and the peak current (i_p) for NVP, NLVP, and NKVP, as shown in Figures S15–16 and 3e, confirms that their electrochemical Na^+ insertion/extraction processes are diffusion-controlled [39]. The Na^+ diffusion coefficients (D_{Na+}) for NVP and NKVP were calculated using the Randles-Sevcik equation (Figure 3f). Specifically, the D_{Na+} values corresponding to Peak1, Peak2, and Peak3 in NKVP were determined to be 8.53×10^{-10}, 2.96×10^{-10} and 1.12×10^{-10} $cm^2 s^{-1}$, respectively. These values significantly exceed those of the redox peaks observed in NVP. Similarly, D_{Na+} obtained by GITT tests are shown in Figure 3g. The ion diffusion coefficients of NKVP are significantly higher than those of NVP, particularly during discharge (Na^+ insertion). Critically, while NVP exhibits severe iR drop and a concomitant sharp plummet in D_{Na+} at 55% Na^+ intercalation stage, NKVP maintains a substantially higher D_{Na+} (one order of magnitude greater on a logarithmic scale), indicating lower migration energy barrier and smaller concentration polarization during the Na^+ (de)intercalation [43]. EIS results (Figure 3h) reveal that the charge transfer resistance (R_{ct}) of NKVP and NVP was nearly identical before cycling at OCV state. However, after 100 cycles at discharged state, NKVP electrode exhibited a significantly smaller R_{ct} value than that of pristine NVP, which can be attributed to the enhanced interfacial stability by K^+ substitution after cycling [51–53].

To gain insight into the preferential K^+ substitution at the Na sites and clarify the performance-enhancing mechanism, density functional theory (DFT) calculations were performed. Two substitution models were constructed by substituting K^+ for Na^+ at either Na1(6b) or Na2(18e) sites while maintaining crystal symmetry, and their total energies were calculated (Figure 4a). Results demonstrate that K^+ occupation of the Na1 site yielded the lowest total energy, i.e., −863.53 eV, lower than that of the Na2 site (−862.06 eV). This indicates superior thermodynamic stability of K^+ at the Na1 site and its preferential occupation under thermodynamic equilibrium, which is consistent with XRD Rietveld refinement results [54, 55]. Thus, the Na1-occupied K^+ substitution model was consequently used for subsequent calculations. Figure S17 depicts the crystal models and their 3D projection schematics of NVP and NKVP. Calculations revealed anisotropic lattice evolution in NKVP with slight contraction of the *a*- and *b*-values but severe expansion of the c-value compared to NVP. The theoretical results coincide with the Rietveld refinement data (Figures 1c and S1 and Table S1), confirming the feasibility of the proposed theoretical crystal model [39]. From the theoretical crystal models, the average length of V-O bonds in NKVP is 2.003 Å, longer than that of NVP (1.994 Å) (Figure 4b). This indicates that the incorporation of K^+ weakens the orbital overlap between V and O, reduces its covalency, and enhances its ionic character, thus improving the redox kinetics [33].

Figures 4c,d and S18 present the migration energy barriers along the identical diffusion pathways of Na^+ in NKVP and NVP. Results reveal that NKVP exhibits a significantly reduced migration barrier of 1.385 eV compared to that of NVP (3.536 eV) within the same diffusion pathway. This indicates that K-substitution at the Na1 site markedly enhances the Na^+ diffusion behaviors, aligning with the improved diffusion coefficients and the interfacial kinetics [33, 39, 56]. Figure 4e,f show the density of states (DOS) distributions of NVP and NKVP. Notably, the O 2p orbitals and the V 3d orbitals form hybridized states near the Fermi energy level (0 eV) in both materials, with their DOS maxima crossing the Fermi level. This similarity indicates a comparable intrinsic electronic conduction mechanism in NVP and NKVP [39, 54, 55], suggesting that the substitution of K^+ ions at Na1 sites does not affect the intrinsic electronic structure in NASICON materials, i.e., the electronic conductivity of NKVP is not significantly affected. This is consistent with the conclusions obtained from the EIS spectra in Figure 3h. Nevertheless, the significantly improved ion migration kinetics ultimately enhanced the sodium storage performance of the material, leading to better rate capability and energy efficiency.

To understand how K^+ substitution modifies the local bonding environment, the differential charge density (DCD) was analyzed

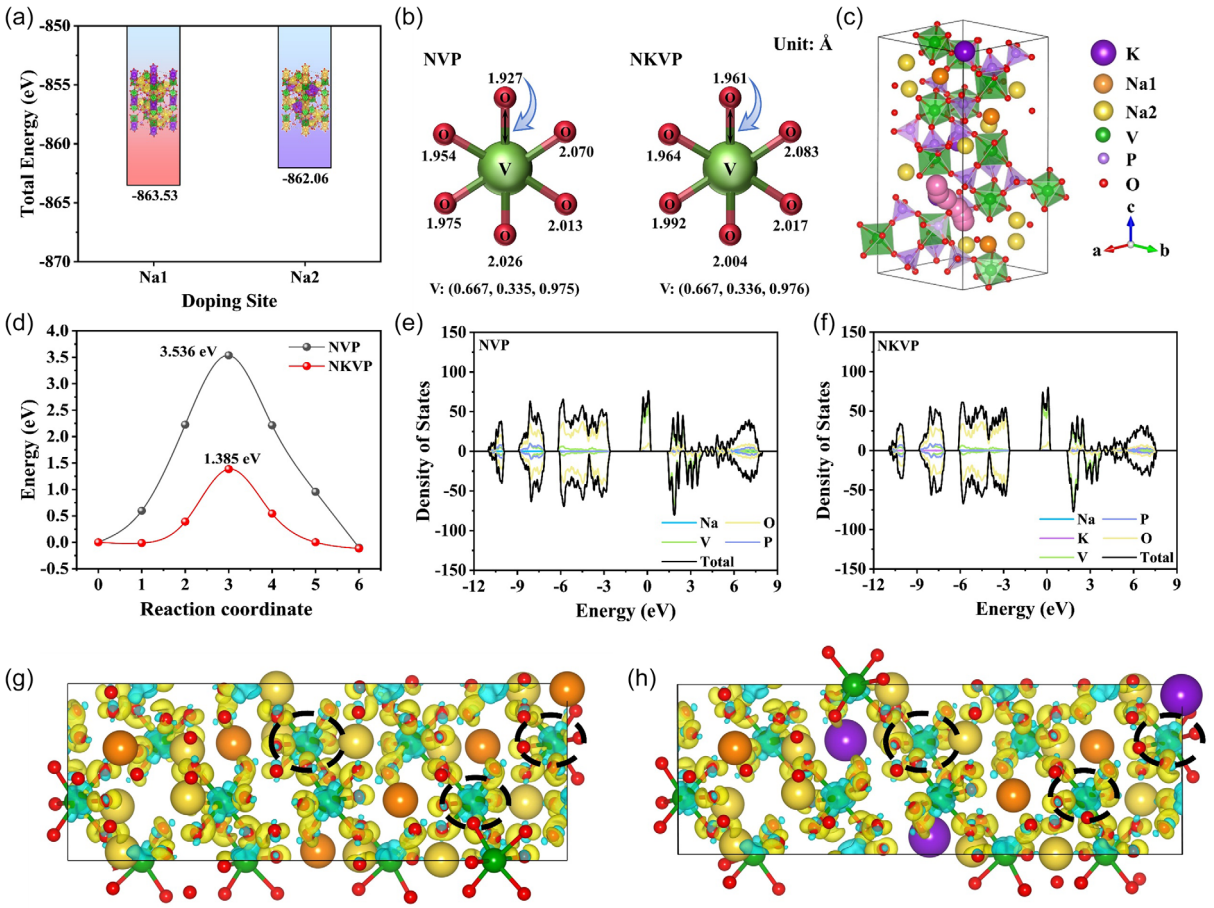

FIGURE 4 | (a) Calculated total energy values for K ions occupying the Na 1 and Na 2 positions, respectively. (b) V–O bond lengths in the theoretical crystal structures of NVP and NKVP. (c,d) Na^+ migration pathways with corresponding migration energy barriers. (e,f) calculated density of states (DOS) and the corresponding partial density of states (pDOS) of NVP and NKVP. (g,h) Charge density distribution of NVP and NKVP (yellow=electron accumulation, blue=electron consumption).

(Figure 4g,h). Comparative analysis reveals the clearly enhanced charge depletion (blue regions) around V atoms in NKVP compared to NVP. This charge redistribution demonstrates that K^+ incorporation facilitates electron transfer from V to O atoms, strengthening the ionic character of V—O bonds [39, 57]. DFT analyses demonstrate that K^+ substitution at the preferential Na sites synergistically improves the sodium storage performance of NVP, which benefits from enhancing structural stability, weakening V—O bond covalency, and lowering Na^+ migration energy barriers. This work confirms that preferential substitution by alkali ion dopants can directionally tune the local bonding environment and diffusion kinetics within stable NASICON frameworks, enabling breakthroughs in high-power, long-life cathodes.

To evaluate the potential of NKVP as a practical cathode material, full cells were fabricated using presodiated hard carbon (HC) anodes (denoted as NKVP//HC) and tested within the 2.5–4.2 V voltage range (Figure 5a). It should be noted that an ether-based electrolyte (1 M $NaPF_6$ in PC/FEC) was also used for the NKVP//HC full-cell tests. The results indicate that the carbonate-based electrolyte led to comparatively poorer rate capability (Figures S19–21), a result attributed to the less favorable interfacial kinetics of the hard carbon anode in that system [58]. Linear sweep voltammetry (Figure S22) confirms that the 1 M $NaPF_6$ in diglyme electrolyte exhibits an onset decomposition voltage of ~4.36 V. This value is well above the 4.2 V upper cut-off used in our full-cell tests, ensuring stable operation within the 2.5–4.2 V window [59]. Figure 5b presents the typical GCD curves of NKVP and HC electrodes in half-cell configuration at 0.5 C. The HC anode delivers a specific capacity of 299.5 mAh g^{-1}, while NKVP exhibits a specific capacity of 103.63 mAh g^{-1}. The N/P ratio in full cell was calculated to be 1.27. The rate performance of NKVP//HC is illustrated in Figure 5c. At C-rates of 0.5C, 1C, 2C, 5C, 10C, 20C, and 30C, the full cell provides specific capacities of 99.92 mAh g^{-1}, 99.80 mAh g^{-1}, 99.60 mAh g^{-1}, 98.43 mAh g^{-1}, 95.33 mAh g^{-1}, 87.56 mAh g^{-1}, and 79.1 mAh g^{-1}, respectively (based on the mass of the cathode), indicating its superior high power capability. Figure 5d displays the GCD curves of NKVP//HC cells at different rates, where the characteristic plateau aligns well with those of NKVP electrodes in the half-cells. The cycling performance of NKVP//HC was also tested as shown in Figure 5e. After precycling three times at 0.5C and cycling for 97 cycles at 5C, a specific capacity of 89.68 mAh g^{-1} was retained, with a capacity retention rate of 97.4%. These results demonstrate that NKVP//HC full cells exhibit outstanding rate capability and cycling stability, underscoring its suitability as a high-power cathode material for practical SIBs.

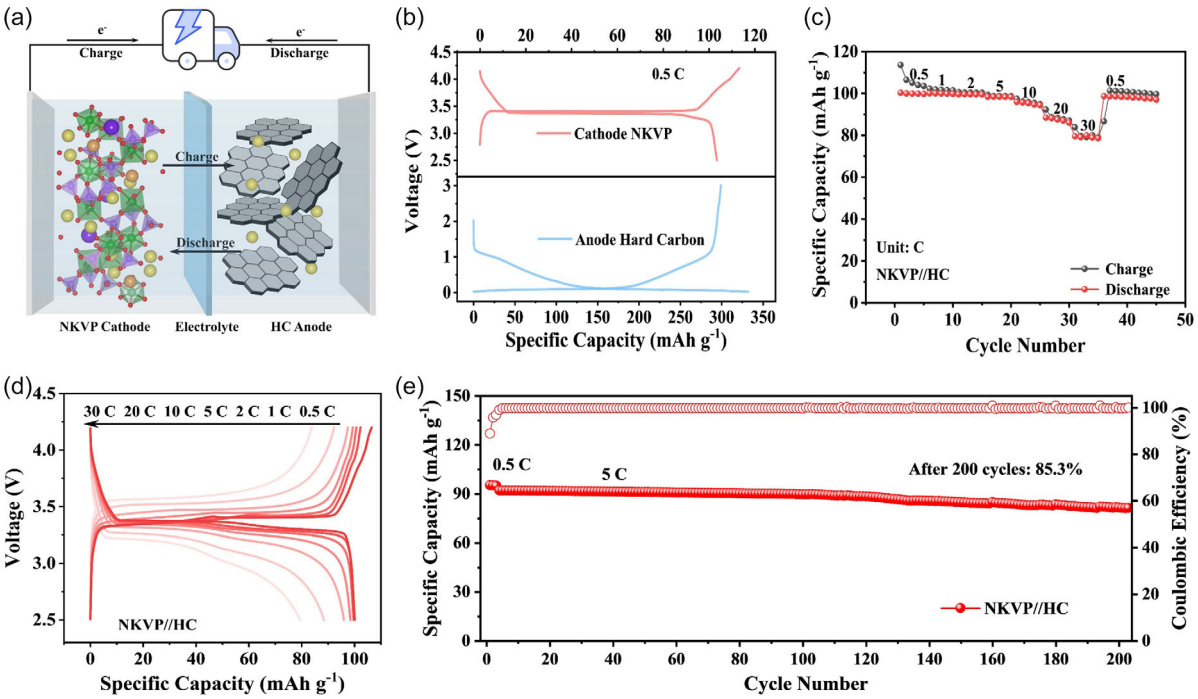

FIGURE 5 | (a) Schematical illustration of an NKVP//HC full cell. (b) GCD curves of NKVP cathode (red) and HC anode (blue) in half cells. (c) Rate performance and (d) corresponding GCD curves. (e) Cycling performance of NKVP//HC full cell at 5C.

3 | Conclusions

In summary, we have successfully synthesized and comprehensively evaluated alkali ion (Li^+, K^+)-substituted NVP as NASICON cathodes for SIBs. Results specifically highlight the superior impact of preferential K^+ substitution at (6b) Na1 sites in unlocking exceptional high-power performance. This targeted substitution effectively broadens Na^+ transport channels and modulates the local bonding environment, significantly alleviating kinetic limitations arising from two-phase reactions and Na^+/vacancy ordering during discharge. Consequently, the K^+-substituted NKVP cathode delivers (at 25 ± 1°C) a reversible capacity of 103.6 mAh g^{-1} at 0.5C, retains 77.8% of its capacity at 100C, and maintains 80.8% capacity over 10,000 cycles at 50C, along with improved high-temperature stability over 3000 cycles at 10C and 60°C. Kinetic analyses confirm that the preferential K^+ substitution enhances the Na^+ diffusion coefficient and reinforces the structural framework, thereby reducing voltage polarization with high energy efficiency and ultralong cycling stability. DFT calculations elucidate the underlying triple mechanism: K^+ substitution synergistically improves structural stability, increases the ionicity of V—O bonds, and lowers the Na^+ migration energy barrier. This fundamental understanding of alkali cation modulation strategy offers deep insights for developing high-power, long-life NASICON electrode materials for SIBs.

Author Contributions

Hongsheng Han: formal analysis (lead), investigation (lead), methodology (lead), writing – original draft (lead), writing – review and editing (supporting). **Ruifu Li:** investigation (supporting), visualization (lead), writing – review and editing (supporting). **Kaidi Wang:** formal analysis (supporting), investigation (supporting), writing – review and editing (supporting). **Hongxu Qu:** data curation (supporting), formal analysis (supporting), writing – review and editing (supporting). **Huihua Li:** data curation (equal), methodology (supporting), resources (lead), validation (lead), writing – review and editing (supporting). **Minghua Chen:** resources (equal), software (lead), validation (supporting), writing – review and editing (supporting). **Huang Zhang:** conceptualization (lead), funding acquisition (lead), project administration (lead), supervision (equal), writing – review and editing (lead). **Stefano Passerini:** conceptualization (supporting), supervision (equal), writing – review and editing (equal).

Acknowledgments

This work was financially supported by the National Natural Science Foundation of China (52307236, 52377214), the China Postdoctoral Science Foundation (2023M730885), and the Postdoctoral Science Foundation of Heilongjiang Province (LBH-Z23197). The basic funding of the Helmholtz Association was also acknowledged.

Open Access funding enabled and organized by Projekt DEAL.

Funding

This work was supported by the Helmholtz Association, the National Natural Science Foundation of China (grant 52307236, 52377214), the China Postdoctoral Science Foundation (grant 2023M730885), and the Heilongjiang Provincial Postdoctoral Science Foundation (grant LBH-Z23197).

Conflicts of Interest

The authors declare no conflicts of interest.

Data Availability Statement

The data that support the findings of this study are available from the corresponding author upon reasonable request.

References

1. R. Usiskin, Y. Lu, J. Popovic, et al., "Fundamentals, Status and Promise of Sodium-Based Batteries," *Nature Reviews Materials* 6, no. 11 (2021): 1020–1035, https://doi.org/10.1038/s41578-021-00324-w.

2. Y. Zeng, J. Xu, Y. Wang, S. Li, D. Luan, and X. W. Lou, "Formation of CuMn Prussian Blue Analog Double-Shelled Nanoboxes Towards Long-Life Zn-Ion Batteries," *Angewandte Chemie International Edition* 61, no. 48 (2022): e202212031, https://doi.org/10.1002/anie.202212031.

3. M. Weiss, R. Ruess, J. Kasnatscheew, et al., "Fast Charging of Lithium-Ion Batteries: A Review of Materials Aspects," *Advanced Energy Materials* 11, no. 33 (2021): 2101126, https://doi.org/10.1002/aenm.202101126.

4. X. X. Zhao, X. T. Wang, J. Z. Guo, et al., "Dynamic Li^+ Capture Through Ligand-Chain Interaction for the Regeneration of Depleted $LiFePO_4$ Cathode," *Advanced Materials* 36, no. 14 (2024): 2308927, https://doi.org/10.1002/adma.202308927.

5. P. Barpanda, L. Lander, S.i Nishimura, and A. Yamada, "Polyanionic Insertion Materials for Sodium-Ion Batteries," *Advanced Energy Materials* 8, no. 17 (2018): 1703055, https://doi.org/10.1002/aenm.201703055.

6. H. Zhang, X. Liu, H. Li, I. Hasa, and S. Passerini, "Challenges and Strategies for High-Energy Aqueous Electrolyte Rechargeable Batteries," *Angewandte Chemie International Edition* 60, no. 2 (2021): 598–616, https://doi.org/10.1002/anie.202004433.

7. D. Larcher and J. M. Tarascon, "Towards Greener and More Sustainable Batteries for Electrical Energy Storage," *Nature Chemistry* 7, no. 1 (2015): 19–29, https://doi.org/10.1038/nchem.2085.

8. D. Wang, X. Bie, Q. Fu, et al., "Sodium Vanadium Titanium Phosphate Electrode for Symmetric Sodium-Ion Batteries with High Power and Long Lifespan," *Nature Communications* 8, no. 1 (2017): 15888, https://doi.org/10.1038/ncomms15888.

9. H. Li, F. Wu, J. Wang, et al., "Anode-Free Sodium Metal Batteries: Optimisation of Electrolytes and Interphases," *Energy & Environmental Science* 18, no. 9 (2025): 3887–3916, https://doi.org/10.1039/D5EE00136F.

10. J. Zhao, H. Lan, G. Yang, et al., "Realizing a 3C Fast-Charging Practical Sodium Pouch Cell," *Angewandte Chemie International Edition* 64, no. 15 (2025): e202501208, https://doi.org/10.1002/anie.202501208.

11. S. W. Kim, D. H. Seo, X. Ma, G. Ceder, and K. Kang, "Electrode Materials for Rechargeable Sodium-Ion Batteries: Potential Alternatives to Current Lithium-Ion Batteries," *Advanced Energy Materials* 2, no. 7 (2012): 710–721, https://doi.org/10.1002/aenm.201200026.

12. P. Zhou, Z. Che, J. Liu, et al., "High-Entropy P2/O3 Biphasic Cathode Materials for Wide-Temperature Rechargeable Sodium-Ion Batteries," *Energy Storage Materials* 57 (2023): 618–627, https://doi.org/10.1016/j.ensm.2023.03.007.

13. H. Gao and J. B. Goodenough, "An Aqueous Symmetric Sodium-Ion Battery with NASICON-Structured $Na_3MnTi(PO_4)_3$," *Angewandte Chemie International Edition* 55, no. 41 (2016): 12768–12772, https://doi.org/10.1002/anie.201606508.

14. J. Peng, B. Zhang, W. Hua, et al., "A Disordered Rubik's Cube-Inspired Framework for Sodium-Ion Batteries with Ultralong Cycle Lifespan," *Angewandte Chemie International Edition* 62, no. 6 (2023): 202215865, https://doi.org/10.1002/anie.202215865.

15. S. Chen, C. Wu, L. Shen, et al., "Challenges and Perspectives for NASICON-Type Electrode Materials for Advanced Sodium-Ion Batteries," *Advanced Materials* 29, no. 48 (2017): 1700431, https://doi.org/10.1002/adma.201700431.

16. R. Huang, D. Yan, Q. Zhang, et al., "Unlocking Charge Transfer Limitation in NASICON Structured $Na_3V_2(PO_4)_3$ Cathode via Trace Carbon Incorporation," *Advanced Energy Materials* 14, no. 21 (2024): 2400595, https://doi.org/10.1002/aenm.202400595.

17. S. Park, Z. Wang, K. Choudhary, et al., "Obtaining $V_2(PO_4)_3$ by Sodium Extraction from Signle-Phase $Na_xV_2(PO_4)_3$ (1<x<3)," *Nature Materials* 24, no. 2 (2025): 234–242, https://doi.org/10.1038/s41563-024-02023-7.

18. R. S. Kate, H. S. Jadhav, U. P. Chothe, et al., "Critical Review of the Recent Progress and Challenges of Polyanion $Na_3V_2(PO_4)_3$ Cathode Materials in Rechargeable Sodium-Ion Batteries," *Journal of Materials Chemistry A* 12, no. 13 (2024): 7418–7451, https://doi.org/10.1039/D3TA07545A.

19. Z. Jian, Y. S. Hu, X. Ji, and W. Chen, "NASICON-Structured Materials for Energy Storage," *Advanced Materials* 29, no. 20 (2017): 1601925, https://doi.org/10.1002/adma.201601925.

20. J. Lee, S. Park, Y. Park, et al., "Chromium Doping into NASICON-Structured $Na_3V_2(PO_4)_3$ Cathode for High-Power Na-Ion Batteries," *Chemical Engineering Journal* 422 (2021): 130052, https://doi.org/10.1016/j.cej.2021.130052.

21. X. Shen, M. Han, Y. Su, M. Wang, and F. Wu, "Alkali Metal Ion Induced Lattice Regulation for All Climate NASICON-Type Cathode with Superior Na-Storage Performance," *Nano Energy* 114 (2023): 108640, https://doi.org/10.1016/j.nanoen.2023.108640.

22. J. Hou, M. Hadouchi, L. Sui, et al. "Insights into Reversible Sodium Intercalation in a Novel Sodium-Deficient NASICON-Type Structure: $Na_{3.40}\Delta_{0.60}Co_{0.5}Fe_{0.5}V(PO_4)_3$," *Small* 19, no. 46 (2023): 2302726, https://doi.org/10.1002/smll.202302726.

23. L. Zhao, H. Zhao, Z. Du, et al., "Computational and Experimental Understanding of Al-Doped $Na_3V_{2-x}Al_x(PO_4)_3$ Cathode Material for Sodium Ion Batteries: Electronic Structure, Ion Dynamics and Electrochemical Properties," *Electrochimica Acta* 282 (2018): 510–519, https://doi.org/10.1016/j.electacta.2018.06.074.

24. Z. Li, C. Sun, M. Li, et al., "$Na_{2.5}VTi_{0.5}Al_{0.5}(PO_4)_3$ as Long Lifespan Cathode for Fast Charging Sodium-Ion Batteries," *Advanced Functional Materials* 34, no. 23 (2024): 2315114, https://doi.org/10.1002/adfm.202315114.

25. C. Jin, Y. Wang, X. Zhao, et al., "Entropy Driving "Quasi-Zero Strain" Stepwise Multicationic Redox Chemistry Towards a High-Performance NASICON-Cathode for Na-Ion Batteries," *Advanced Functional Materials* 35, no. 27 (2025): 2422101, https://doi.org/10.1002/adfm.202422101.

26. M. Li, C. Sun, X. Yuan, et al., "A Configuration Entropy Enabled High-Performance Polyanionic Cathode for Sodium-Ion Batteries," *Advanced Functional Materials* 34, no. 21 (2024): 2314019, https://doi.org/10.1002/adfm.202314019.

27. B. Xing, J. Ren, P. Hu, et al. "Fluoride Doping $Na_3Al_{2/3}V_{4/3}(PO_4)_3$ Microspheres as Cathode Materials for Sodium-Ion Batteries with Multielectron Redox," *Small* 20, no. 29 (2024): 2310997, https://doi.org/10.1002/smll.202310997.

28. C. Xu, J. Zhao, E. Wang, et al., "A Novel NASICON-Typed $Na_4VMn_{0.5}Fe_{0.5}(PO_4)_3$ Cathode for High-Performance Na-Ion Batteries," *Advanced Energy Materials* 11, no. 22 (2021): 2100729, https://doi.org/10.1002/aenm.202100729.

29. L. Deng, F.-D. Yu, Y. Xia, et al. "Stabilizing Fluorine to Achieve High-Voltage and Ultra-Stable $Na_3V_2(PO_4)_2F_3$ Cathode for Sodium Ion Batteries," *Nano Energy* 82 (2021): 105659, https://doi.org/10.1016/j.nanoen.2020.105659.

30. T. Yang, Z. Wu, X. Xu, et al., "Cation-Anion Co-Doped $Na_3V_2(PO_4)_3$ Cathode for Robust and High-Performance Sodium-Ion Storage," *Small Methods* (2025), https://doi.org/10.1002/smtd.202500370.

31. L. Shen, Y. Li, C. Hu, et al., "A High-Rate Cathode Material Based on Potassium-Doped $Na_3V_2(PO_4)_3$ for High/Low-Temperature Sodium-Ion Batteries," *Materials Today Chemistry* 30 (2023): 101506, https://doi.org/10.1016/j.mtchem.2023.101506.

32. Z. Jian, W. Han, X. Lu, et al., "Superior Electrochemical Performance and Storage Mechanism of $Na_3V_2(PO_4)_3$ Cathode for Room-Temperature Sodium-Ion Batteries," *Advanced Energy Materials* 3, no. 2 (2013): 156–160, https://doi.org/10.1002/aenm.201200558.

33. S. Wang, S. Xiong, Z. Li, et al. "Constructing Multi-Electron Reactions by Doping Mn^{2+} to Increase Capacity and Stability in $K_{3.2}V_{2.8}Mn_{0.2}(PO_3)_4/C$ of Phosphate Cathodes for Potassium-Ion

Batteries," *Small* 20, no. 46 (2024): 2308628, https://doi.org/10.1002/smll.202308628.

34. Y. Liu, X. Rong, R. Bai, et al., "Identifying the Intrinsic Anti-Site Detect in Manganese-Rich NASICON-Type Cathodes," *Nature Energy* 8, no. 10 (2023): 1088–1096, https://doi.org/10.1038/s41560-023-01301-z.

35. W. Liu, W. Cui, C. Yi, et al., "Understanding Pillar Chemistry in Potassium-Containing Polyanion Materials for Long-Lasting Sodium-Ion Batteries," *Nature Communications* 15, no. 1 (2024): 9889, https://doi.org/10.1038/s41467-024-54317-8.

36. R. Thirupathi, V. Kumari, S. Chakrabarty, and S. Omar, "Recent Progress and Prospects of NASICON Framework Electrodes for Na-Ion Batteries," *Progress in Materials Science* 137 (2023): 101128, https://doi.org/10.1016/j.pmatsci.2023.101128.

37. J. Bodart, N. Eshraghi, T. Carabin, et al., "Spray-Dried $K_3V(PO_4)_2$/C Composites as Novel Cathode Materials for K-Ion Batteries with Superior Electrochemical Performance," *Journal of Power Sources* 480 (2020): 229057, https://doi.org/10.1016/j.jpowsour.2020.229057.

38. Q. Deng, F. Liu, X. Wu, C. Li, W. Zhou, and B. Long, "An Aqueous BiI_3-Zn Battery with Dual Mechanisms of Zn^{2+} (De)intercalation and I-/I_2 Redox," *Journal of Energy Chemistry* 89 (2024): 670–678, https://doi.org/10.1016/j.jechem.2023.10.035.

39. X. Hu, H. Li, Z. Wang, et al., "High Entropy Helps $Na_4Fe_3(PO_4)_2P_2O_7$ Improve Its Sodium Storage Performance," *Advanced Functional Materials* 35, no. 2 (2025): 2412730, https://doi.org/10.1002/adfm.202412730.

40. S. Park, Z. Wang, Z. Deng, et al. "Crystal Structure of $Na_2V_2(PO_4)_3$, An Intriguing Phase Spotted in the $Na_3V_2(PO_4)_3$-$Na_1V_2(PO_4)_3$ system," *Chemistry of Materials* 34, no. 1 (2021): 451–462, https://doi.org/10.1021/acs.chemmater.1c04033.

41. F. Li, Y.-E. Zhu, J. Sheng, L. Yang, Y. Zhang, and Z. Zhou, "GO-Induced Preparation of Flake-Shaped $Na_3V_2(PO_4)_3$@rGO as High-Rate and Long-Life Cathodes for Sodium-Ion Batteries," *Journal of Materials Chemistry A* 5, no. 48 (2017): 25276–25281, https://doi.org/10.1039/C7TA07943E.

42. K. Saravanan, C. W. Mason, A. Rudola, K. H. Wong, and P. Balaya, "The First Report on Excellent Cycling Stability and Superior Rate Capability of $Na_3V_2(PO_4)_3$ for Sodium Ion Batteries," *Advanced Energy Materials* 3, no. 4 (2013): 444–450, https://doi.org/10.1002/aenm.201200803.

43. C. Sun, Q. Ni, M. Li, et al., "Improving Rate Performance by Inhibiting Jahn-Teller Effect in Mn-Based Phosphate Cathode for Na-Ion Batteries," *Advanced Functional Materials* 34, no. 7 (2023): 2310248, https://doi.org/10.1002/adfm.202310248.

44. H. Zhang, I. Hasa, D. Buchholz, B. Qin, and S. Passerini, "Effects of Nitrogen Doping on the Structure and Performance of Carbon Coated $Na_3V_2(PO_4)_3$ Cathodes for Sodium-Ion Batteries," *Carbon* 124 (2017): 334–341, https://doi.org/10.1016/j.carbon.2017.08.063.

45. X. Xiang, K. Zhang, and J. Chen, "Recent Advances and Prospects of Cathode Materials for Sodium-Ion Batteries," *Advanced Materials* 27, no. 36 (2015): 5343–5364, https://doi.org/10.1002/adma.201501527.

46. C. Che, F. Wu, Y. Li, et al., "Challenges and Breakthroughs in Enhancing Temperature Tolerance of Sodium-Ion Batteries," *Advanced Materials* 36, no. 28 (2024): 2402291, https://doi.org/10.1002/adma.202402291.

47. K. B. Hueso, M. Armand, and T. Rojo, "High Temperature Sodium batteries: Status, Challenges and Future Trends," *Energy & Environmental Science* 6, no. 3 (2013):734, https://doi.org/10.1039/c3ee24086j.

48. Y. Zhou, X. Zhang, Y. Liu, et al. "A High-Temperature Na-Ion Battery: Boosting the Rate Capability and Cycle Life by Structure Engineering," *Small* 16, no. 7 (2020): 1906669, https://doi.org/10.1002/smll.201906669.

49. Y. Li, Y. Mei, H. Liu, et al., "Functional Carbon Dots Induced Defect Configuration Entropy Strengthening Polyanion Cathode for Ultrafast-Charging Sodium Ion Batteries in a Wide Temperature," *Nano Energy* 130 (2024): 110107, https://doi.org/10.1016/j.nanoen.2024.110107.

50. P. Hu, T. Zhu, C. Cai, et al., "A High-Entropy NASICON-Type $Na_{3.2}MnTi_{0.8}V_{0.2}(PO_4)_3$ Cathode Material with Reversible 3.2-Electron Redox Reaction for Sodium-Ion Batteries," *Angewandte Chemie International Edition* 62, no. 14 (2023): 202219304, https://doi.org/10.1002/anie.202219304.

51. L. Wang, J. Wang, L. Wang, et al., "Synergistic Strain Suppressing and Interface Engineering in $Na_4MnV(PO_4)_3$/C for Wide-Temperature and Long-Calendar-Life Sodium-Ion Storage," *ACS Nano* 18, no. 16 (2024): 10863–10873.

52. C. Xu, R. Xiao, J. Zhao, et al., "Mn-Rich Phosphate Cathodes for Na-Ion Batteries with Superior Rate Performance," *ACS Energy Letters* 7, no. 1 (2021): 97–107, https://doi.org/10.1021/acsenergylett.1c02107.

53. Y. Xi, X. Wang, H. Wang, et al., "Optimizing the Electron Spin States of $Na_4Fe_3(PO_4)_2P_2O_7$ Cathodes via Mn/F Dual-Doping for Enhanced Sodium Storage," *Advanced Functional Materials* 34, no. 16 (2023): 2470087, https://doi.org/10.1002/adfm.202309701.

54. J. Cong, S.-h. Luo, P.-y. Li, K. Li, P.-w. Li, and S.-x. Yan, "Towards Enhanced Structural Stability by Investigation of the Mechanism of K Ion Doping in $Na_3V_2(PO_4)_3$/C for Sodium Ion Batteries," *Journal of Energy Storage* 72 (2023): 108808, https://doi.org/10.1016/j.est.2023.108808.

55. J. Li, Q. Yuan, J. Hao, et al., "Boosted Redox Kinetics Enabling $Na_3V_2(PO_4)_3$ with Excellent Performance at Low Temperature through Cation Substitution and Multiwalled Carbon Nanotubes Cross-Linking," *Inorganic Chemistry* 62, no. 43 (2023): 17745–17755, https://doi.org/10.1021/acs.inorgchem.3c02457.

56. H. Li, Y. Wang, X. Zhao, et al., "A Multielectron-Reaction and Low-Strain $Na_{3.5}Fe_{0.5}VCr_{0.5}(PO_4)_3$ Cathode for Na-Ion Batteries," *ACS Energy Letters* 8, no. 9 (2023): 3666–3675, https://doi.org/10.1021/acsenergylett.3c01183.

57. L. Zhu, S. Xiang, M. Wang, et al., "Heterogeneous NASICON-Type Cathode with Reversible Multielectron Reaction for High-Performance Sodium-Ion Batteries," *Advanced Materials* 37, no. 23 (2025): 2408918, https://doi.org/10.1002/adma.202408918.

58. X. Yin, Z. Wang, Y. Liu, et al., "Insight into the Influence of Ether and Ester Electrolytes on the Sodium-Ion Transportation Kinetics for Hard Cabon," *Nano Research* 16, no. 8 (2023): 10922–10930, https://doi.org/10.1007/s12274-023-5793-9.

59. S. Li, M. Jin, X. Song, et al., "Revisiting Ether Electrolytes for High-Voltage Sodium-Ion Batteries," *Energy Storage Materials* 73 (2024): 103815, https://doi.org/10.1016/j.ensm.2024.103815.

Supporting Information

Additional supporting information can be found online in the Supporting Information section. **Supporting Fig. S1:** Rietveld refined XRD pattern of NVP. **Supporting Fig. S2:** Rietveld refined XRD pattern of NLVP. **Supporting Fig. S3:** SEM image of NVP. **Supporting Fig. S4**: Rate performance of half-cells at various current rates from 0.5C to 100C. **Supporting Fig. S5:** Rate performance of NKVP from independent replicate half-cell tests. **Supporting Fig. S6:** GCD curves of NVP half-cells at different current rates from 0.5C to 50C. **Supporting Fig. S7:** GCD curves of NLVP at different current rates from 0.5C to 50C. **Supporting Fig. S8:** Rate performance of NVP and NKVP cathodes at a high mass loading (5 mg cm^{-2}). **Supporting Fig. S9:** Energy efficiency of NVP, NLVP and NKVP half-cells at different rates from 0.5C to 50C. **Supporting Fig. S10:** Ex-situ XPS spectra in the V 2p region of NVP pristine and after the charge step. **Supporting Fig. S11:** XPS survey spectrum of pristine NVP electrode. **Supporting Fig. S12:** XPS survey spectrum of pristine NKVP electrode. **Supporting Fig. S13:** CV curves of an NVP half-cell at different scan rates. **Supporting Fig. S14:** CV curves of an NLVP half-cell at different scan rates (the strongest peak during discharge is defined as Peak 2). **Supporting Fig. S15:** Linear relationship between

the square root of the scanning rate ($v^{1/2}$) and the peak current (i_p) of NVP. **Supporting Fig. S16:** Linear relationship between the square root of the scanning rate ($v^{1/2}$) and the peak current (i_p) of NLVP. **Supporting Fig. S17:** Theoretical crystal model of (a) NVP and (b) NKVP. **Supporting Fig. S18:** Illustration of Na+ migration path in the NVP structure. **Supporting Fig. S19:** Charge-discharge curves of the NKVP and hard carbon (HC) anode, measured in half-cells using the 1 M NaPF6 in PC with 5 vol% FEC electrolyte. **Supporting Fig. S20**. Rate performance of the NKVP full cell employing 1 M NaPF6 in PC with 5 vol% FEC as the electrolyte, tested from 0.5 C to 30 C. **Supporting Fig. S21:** GCD curves of NKVP full-cell at different current rates from 0.5 C to 30 C. **Supporting Fig. S22:** LSV curves of Na//Al cells with 1 M NaPF6 in diglyme tested at 1 mV s^{-1} from 2.5 V to 5.5 V. **Supporting Table S1:** Lattice parameters of NVP, NLVP and NKVP from Rietveld refinement. **Supporting Table S2:** Refined atomic occupancies in $Na_3V_2(PO_4)_3$. **Supporting Table S3:** Refined atomic occupancies in $Na_{2.5}Li_{0.5}V_2(PO_4)_3$. **Supporting Table S4:** Refined atomic occupancies in $Na_{2.5}K_{0.5}V_2(PO_4)_3$.